DES of a Slingsby Firefly Aircraft: Unsteady Flow Feature Extraction Using POD and HODMD

Corrochano, A., Neves, A. F., Khanal, B., Le Clainche, S. & Lawson, N. J

Original citation & hyperlink:

Corrochano, A, Neves, AF, Khanal, B, Le Clainche, S & Lawson, NJ 2022, 'DES of a Slingsby Firefly Aircraft: Unsteady Flow Feature Extraction Using POD and HODMD', Journal of Aerospace Engineering, vol. 35, no. 5.

https://doi.org/10.1061/(asce)as.1943-5525.0001457

DOI 10.1061/(asce)as.1943-5525.0001457

ISSN 0893-1321

ESSN 1943-5525

Publisher: American Society of Civil Engineers

DES of a Slingsby Firefly Aircraft: Unsteady Flow Feature Extraction using POD and HODMD

Adrián Corrochano[1], Ana F. Neves[2], Bidur Khanal[3], Soledad Le Clainche[4], and Nicholas J. Lawson[5]

[1]School of Aerospace Engineering, Universidad Politécnica de Madrid, E-28040, Spain.
Email: adrian.corrochanoc@upm.es

[2]Cranfield University, Cranfield, Bedfordshire. MK43 0AL

[3]Coventry University, Priory Street, Coventry, United Kingdom, CV1 5FB

[4]School of Aerospace Engineering, Universidad Politécnica de Madrid, E-28040, Spain.

[5]Cranfield University, Cranfield, Bedfordshire. MK43 0AL

ABSTRACT

In this paper, Higher-Order Dynamic Mode Decomposition (HODMD) has been applied to find the main patterns and frequencies of a transient aerodynamic flow field when an aircraft wing experiences stall. This method has been applied to a computational flow simulation with a turbulence model based on a hybrid RANS/LES (commonly known as Detached-Eddy Simulation [DES]), where a combination of 2D and 3D flow visualization techniques are used to understand the vortex shedding from the main wing and its interaction with the tailplane. Simulation results have been compared to the experimental ones and the results with POD have been compared with the HODMD analysis. The main advantage of HODMD resides in its identification of the main physical phenomena and the most relevant instabilities that lead the fluid dynamics. New flow control strategies can be defined when the underlying physics and the flow dynamics are known. Moreover, HODMD is robust in noisy and turbulent databases using less data than FFT, which gives potential for future flow control applications, focused on improving the aircraft's efficiency.

INTRODUCTION

Aircraft design is an evolving area and with the availability of advanced numerical techniques such as finite element methods and computational fluid dynamics (CFD), it is now possible to do an initial detailed design virtually (Raymer 1999; Okonkwo and Smith 2016; Rizzi et al. 2010). A challenging area of any design is the prediction of aerodynamic coefficients during and beyond aircraft stall (Ciliberti et al. 2017; Lutz et al. 2015; Grote and Radespiel 2006; Teng et al. 2015; Lutz et al. 2016; Teng et al. 2016). More specifically, the pitching moment and lift and drag coefficients have complex characteristics (Phillips 2010), which at high angles of attack may change significantly post-stall, in some cases leading to an autorotation and the development of a spin (Rao and Go 2019; Bennett and Lawson 2018).

The complex nature of the coefficients and the possibility of spin generally lead to a requirement for extensive wind tunnel and flight testing (Hall et al. 2004) to verify the behaviour of the aircraft in a heavy stall (Heinz 2020). Recent developments of advanced numerical methods, such as Detached Eddy Simulation (DES) and unsteady RANS methods (Zhou et al. 2019a; Zhou et al. 2019b), now offer the opportunity to predict these complex aerodynamic behaviours with greater fidelity (Wang and Fu 2017; Casadei et al. 2019; Neves et al. 2020), supplementing the existing experimental data and providing design fixes, ahead of the flight testing program.

Where DES-based turbulence modelling is widely used in 3D transient simulations, it is necessary to highlight the limitations of Reynolds-Averaged Navier-Stokes (RANS) approaches. Several computational studies in the past have experienced a common limitation with RANS solver and turbulence models applied to unsteady flows (Spalart and Allmaras 1997; Nichols 2006; Sinha et al. 1998). The RANS solver produces increased eddy viscosity which causes excessive damping of the unsteadiness of the flow field. Spatially filtered models such as Large-Eddy Simulation (LES) have provided improved results for simulating unsteady flows. LES models, however, are currently limited to low Reynolds numbers because of the computing resources required to resolve the small-scale turbulent structures. LES is not yet, therefore, a feasible tool for the simulation of highly transient 3D flow fields.

In recent years, hybrid methods, which behave as a standard RANS model within the attached boundary layer and as an LES Sub-Grid Scale model in the rest of the flow (more commonly known as DES), have been increasingly used to address this problem (Spalart et al. 2006; Menter 1994; Menter and Kuntz 2003). A hybrid RANS/LES model, based on the $k-\omega$ SST formulation (Menter 1994; Menter and Kuntz 2003), was therefore chosen for this research. This type of model improves the turbulent flow predictions in the regions with significant separated flows.

DES Method

As explained above, the DES is essentially a hybrid LES/RANS model, which uses the standard RANS formulation within the attached boundary layers and activates an LES Sub-Grid Scale type model in the rest of the flow, including the separated regions. A typical DES simulation has been known to significantly reduce the computational resources required for the high-Reynolds number wall-bounded flows, where using a full LES modelling would be prohibitively expensive. In the DES formulation, the standard RANS length scale is replaced with a DES length scale defined as follows.

The length scale for the RANS turbulence model $k-\omega$ SST, in terms of the turbulence kinetic energy k and the specific dissipation rate ω, can be written as:

$$l_{k-\omega} = \frac{k^{1/2}}{\beta^* \omega}, \tag{1}$$

For the DES formulation, the length scale in the standard RANS equation is replaced by a DES length scale, $\tilde{l}$, which is calculated as:

$$\tilde{l} = min(l_{k-\omega}, C_{DES}\Delta), \tag{2}$$

and $\Delta = max(\Delta x, \Delta y, \Delta z)$.

Here C_{DES} is a calibrated constant for the DES model (it is equal to 0.61), and Δ is the largest cell dimension in the local grid. The modified length scale, calculated using the relation in eq. 2, ensures a length scale that is the same as the standard RANS length scale near the walls, where $l_{k-\omega} \ll \Delta$ and reduces to the local grid spacing away from the walls, where $l_{k-\omega} \gg \Delta$. The effect of this is to activate a hybrid turbulence model that behaves as a standard RANS model within the attached boundary layers and as an LES Sub-Grid Scale model in the rest of the flow, including the separated regions.

POD and DMD Methods

In addition to the CFD, to simulate transient aerodynamic flow fields, several computational techniques have been developed, which aid in the extraction of flow features and interpretation of complex flow characteristics. The main goal of such methods is to decompose the flow as an expansion of hierarchical modes, which describe the main flow dynamics using a reduced basis of modes. Using this information, it is possible to identify the main patterns driving the flow dynamics. These patterns lead the main flow instabilities producing changes in the flow (i.e.: transition from laminar to turbulent flow, drag increasing or drag reduction, heat transfer enhancement, et cetera). The patterns can also be used to construct reduced order models, to reproduce or predict the flow dynamics with a reduced computational cost (in terms of memory and computational time). Two such techniques, which are proving increasingly popular in the complex aerodynamic flow fields, are proper orthogonal decomposition (POD) and dynamic mode decomposition (DMD) (Vega and Le Clainche 2021; Berkooz et al. 1993). POD and DMD methods have seen application in the analysis of turbulent flow flows (Chen et al. 2012; Hu et al. 2020), or non-linear dynamical systems and poor-quality experimental data (Le Clainche and Vega 2017b; Higham et al. 2016; Le Clainche et al. 2017a). These decomposition methods also offer the possibility of flow forecasting in compressible flows (Rona and Brooksbank 2003), or other complex fluid flows (Howard et al. 2017; Gardner et al. 2019). The ability to forecast unsteady flows with POD or DMD may allow incorporation into an advanced flow control system for aerodynamic stall (Frankhouser et al. 2015), or control other aerodynamic phenomena in-flight (Alexander et al. 2016), where POD or DMD methods would allow prediction of the onset of different aerodynamic characteristics. Higher-order dynamic mode decomposition (HODMD) (Le Clainche and Vega 2017a) is an extension of DMD, introduced for the identification of flow patterns in complex turbulent data (Le Clainche et al. 2020) and experiments with noisy data (Le Clainche et al. 2017b). The accuracy and validity of the method have been tested in complex and realistic aerodynamic flow fields, identifying the evolution of crossflow instabilities (Le Clainche et al. 2019) and predicting flutter flight test (Mendez et al. 2021) (see more examples in (Vega and Le Clainche 2021)). Furthermore, work has been completed in the identification of the main dynamics of the dynamic stall. In this case, (Mohan et al. 2015) explored the flow structures and frequencies driving the dynamic stall using POD and DMD. Moreover, (Mallik and Raveh 2020) applied these techniques to a NACA 0012 airfoil to study the aerodynamic damping due to light dynamic stall.

Previous work by the authors (Neves et al. 2020), has demonstrated how a DES model can correctly predict the aerodynamic behaviour in a heavy stall. In that initial work, basic validation measurements were used to check the DES model, by observing the buffet behaviour during the stall. Initial observations from the DES model showed an extensive unsteady wake, with evidence of a wake-tailplane interaction.

In this paper, one of the key aims is to use 3D flow visualisation techniques to extract, analyse and interpret the complex vortical structures in the DES data, which are shed from the main wing in stall, and travel downstream to interact with the tailplane. Moreover, POD and HODMD methods are used to assess their application in capturing the distribution of the unsteady energy spectrum and the reconstruction of the unsteady flow snapshots. The other key aim of the present study is to understand and assess the application of data-driven methods (POD and HODMD), in analyzing the energy content of unsteady vortical structures shed from the aircraft wing and control surfaces, and identifying the main frequencies leading the flow dynamics, which can be connected with flow instabilities (Le Clainche et al.

2020).

To meet these aims, a full 3D CFD simulation, using two-equation DES turbulence modelling will be performed and the resulting transient CFD data will be processed using POD and HODMD techniques, to extract dominant frequency modes in the unsteady fluctuations. The frequency characteristics captured will be cross-checked with the 3D vortex shedding identified from the spectral analysis, as well as from the experimental measurements.

NUMERICAL SIMULATIONS

CFD Modelling

Previous work by the authors described the DES model based on $k-\omega$ SST formulation, and its application in modelling the unsteady flow field around the Slingsby in the stalled condition (Neves et al. 2020). The following section summarises the main details of the CFD simulation and outlines the additional data extracted from the computed unsteady flow field, to apply the proper orthogonal decomposition (POD) and HODMD methods to the DES wake data.

Pre-processing and Geometrical Setup for the CFD Simulation

A half model of a Slingsby Firefly geometry was meshed using the CFD pre-processor in ANSYS, ANSYS ICEM CFD. A 3D fluid domain in a semi-cylindrical topology was chosen for generating the computation mesh. To ensure that the computed flow field was not influenced by the domain boundaries and based on previous studies (Lawson et al. 2017), the boundaries were set to be at least 10 times the largest characteristic length of the body being studied, with a pressure field domain boundary. A hybrid mesh was generated initially with a top-down approach Octree method, with prism layers representing the boundary layer. The final mesh was computed with the Delaunay method, a bottom-up approach that requires an initial surface mesh, which was set as triangular in this case with prisms and tetrahedra for the fluid volume.

The final computational domain had an overall mesh size of 11.3 million cells, Figure

1a shows the aircraft geometry and a cross-sectional view of the mesh generated. Here the isotropic cells are visible around the main wing and extend a considerable distance downstream to cover the aircraft tailplane. These cells ensure the DES model can be activated in this region. For the prism layers in the mesh, an initial height and total height were set so that the three regions of the turbulent boundary layer, namely, the viscous layer, the buffer layer and the log-law region, were adequately modelled. To achieve this, the prism layers were designed to contain a cell inflation layer of $y^+ < 1$ to $y^+ = 1000$. Since in this work the region of interest is the wing's wake where the vortex shedding occurs, the grid cells behind the main wing were maintained close to isotropic volumes with a minimum amount of cell stretching so that an LES-type length scale is invoked in this region. All the solid surfaces were treated as adiabatic walls with a no-slip condition. For the solution, an implicit density-based solver was run using a $k - \omega$ SST turbulence model, with the DES solution initialised from a RANS solution with a convergence of 10^{-4} for globally scaled residuals. The DES solution was run with a time step of 6.7×10^{-4}s and 20 iterations per time step.

The spatial discretization used in the simulations was finite volume method (default option for compressible flow in Fluent), with a second-order central differencing applied to the modified turbulent viscosity and a second-order implicit scheme was adopted for the temporal discretization. The density-based solver option was chosen to ensure a fully compressible solution and a constant time step of 6.7×10^{-4}s was maintained for the unsteady simulation (a constant time step is essential for the time consistency of the resolved unsteady structures especially in DES simulations). The time step size for the simulation was setted after considering the smallest shedding frequency of interest in this case, and also in agreement with the literature of Spalart on DES modelling (Spalart 2001). Furthermore, each transient solution at each time step was resolved by applying 20 subiterations. The simulations were run initially for a total of 8000 time steps (stable unsteady flow characteristics were achieved by this time) for fully resolved unsteady structures. Then the unsteady pressure monitors were activated and the flow simulations were run for further 8500 time steps, to study the spectral contents of the pressure signals at various locations. Further details on the mesh generation and the CFD setup can be found in (Neves et al. 2020).

FLIGHT TEST DATA

This section summarises previous flight test work by the authors (Neves et al. 2020) which was taken from a $T67M260$ Slingsby Firefly light aircraft and used to validate the DES model. The flight tests were designed to aerodynamically stall the aircraft, whilst accelerometer, video and surface flow data were recorded. Additional ground tests were also completed to establish resonant structural modes of the tailplane structure. The latter work was completed, as videos taken during the flight indicated a strong interaction of the wing wake with the tailplane structure. This video data and the data processing methods used to measure the tailplane behaviour in the stall will be the subject of a separate paper.

An example of normal axes Pixhawk4 accelerometer and spectra data at $250Hz$, taken from a stall sequence, are shown in Figure 2. The sequence is timed from the initiation of the Pixhawk4 unit and significant stages are indicated in the sequence, as confirmed from accompanying video data in the flight. In the first stage of the sequence, shown in Figure 2a, the engine idle frequency of $1050rpm$ ($17.5Hz$) dominates the spectra. Around $1.5s$ later, the aircraft is stalled and the dominant frequencies switch from the engine to the aerodynamic and structural interactions, indicated in Figure 2b, where the tailplane structural natural frequencies are excited at $9.4Hz$ and $40.5Hz$. In this case, the DES model was predicting aerodynamic wake shedding frequencies close to the lower frequency of the tailplane structure (Neves et al. 2020), as confirmed by the video footage of the tail. In the last two stages of the sequence, a large change and reduction in acceleration can be seen which coincides with the 'wing drop' in a heavy stall. This phenomenon is the initial stage of a wing autorotation. However, in the final stage, the pilot has prevented this from occurring and has started the recovery from the stall to normal flight, where engine power has now been added, as evidenced by the return of the dominant frequency of the engine in the spectra (see Figure 2c), as also seen in the first stage in Figure 2a.

METHODOLOGY

This section introduces the two data-driven techniques to analyse the data obtained in the numerical simulations. We use Proper Orthogonal Decomposition (POD) and Higher-Order Dinamic Mode Decomposition (HODMD), which are techniques that provide complementary information. HODMD can find the main dynamics of the system while POD identify modes based on the kinetic energy. Each POD mode is associated to multiple frequencies, while each DMD mode oscillate with a single frequency. For simplicity, the data are organized in matrix form. Let

$$\mathbf{P} = [\mathbf{p_1}, \mathbf{p_2}, \mathbf{p_3}, \ldots, \mathbf{p_K}], \tag{3}$$

be a matrix of K snapshots, where $\mathbf{p_i}$ represents the pressure field in the flow or the velocity vector components (or the two of them, concatenated in rows). In this article, the first methodology only uses the pressure field, where each column is a vector of length M, formed by the pressure field from each snapshot, where M is the number of grid points forming the computational mesh. In the data analysed in this article $M < K$, hence the rank of $\mathbf{P}$ is $N \leq K$. In the other methodology presented, both the pressure and velocity fields are concatenated in rows, where each column is a vector of length $4M$ (the pressure field and the three velocity components). The summary of the steps implemented on the methodology can be found in Figure 3.

Proper Orthogonal Decomposition

Proper Orthogonal Decomposition (POD) is a technique used to decompose a random vector or scalar field into a set of deterministic functions or modes. Its origin can be traced to the field of turbulence, when it was first introduced by Lumley (Lumley 1967). The decomposed functions of the POD modes contain valuable information on the characteristics of the unsteady flows. In particular, the POD is used to identify the coherent structures in turbulent flows, which are generally difficult to define and observe.

The POD method involves decomposing the original vector or scalar field into a sum of weighted basis functions, and the functions are computed from the original flow field data, more specifically, from the fluctuating flow field. The formation of the basis functions is from statistical correlation and contains normalized basis functions, which are orthogonal among them. Here, only the mathematical background relevant to the main POD concept and the approach used to reconstruct the snapshot of the flow field are given. A more comprehensive coverage on the method can be found in the literature (Chatterjee 2000; Sirovich 1987; Cordier and Bergmann 2008).

As an illustration, the POD approach of analysing a known pressure history is presented. The main goal is to construct a set of time-independent POD bases that maximise the L2 norm representing the pressure field in the flow. Based on the snapshot matrix eq.3, a correlation matrix $\mathbf{C}$ can then be formed by,

$$\mathbf{C} = \tilde{\mathbf{P}}^T \tilde{\mathbf{P}}, \tag{4}$$

where $\tilde{\mathbf{P}}$ is obtained by recasting the matrix $\mathbf{P}$ to give a zero mean value, i.e.,

$$\tilde{\mathbf{P}} = \left[\mathbf{p}_1 - \bar{\mathbf{p}}, \mathbf{p}_2 - \bar{\mathbf{p}}, \mathbf{p}_3 - \bar{\mathbf{p}}, \ldots, \mathbf{p}_K - \bar{\mathbf{p}}\right], \tag{5}$$

where $\bar{\mathbf{p}} = \left(\sum_{i=1}^{K} \mathbf{p}_i\right)/K$. It should be noted that these snapshots do not necessarily need to be equidistant in time for proper performance of this technique. A singular value decomposition rearranges C in the following matrix product:

$$\mathbf{C} = \mathbf{V}\boldsymbol{\Lambda}\mathbf{V}^T, \tag{6}$$

where the diagonal matrix $\boldsymbol{\Lambda}$ in eq.6 contains the eigenvalues $[\lambda_1, \lambda_2, \lambda_3, \ldots, \lambda_N]$ of $\mathbf{C}$, $\mathbf{V}$ is the matrix of the associated eigenvectors, which are connected to the POD modes (organized in columns) as presented below, and the eigenvalues, $\lambda_1 \geq \lambda_2 \geq \lambda_3 \geq \ldots \geq \lambda_N$, represent the energy content associated to each POD mode. Thus, the POD modes are ordered from the most energetic to the smallest energy content.

A proper orthogonal decomposition basis function, $\mathbf{\Phi} = [\phi_1, \ \phi_2, \ \phi_3, \ \ldots, \ \phi_N]$ is then described as,

$$\mathbf{\Phi} = \tilde{\mathbf{P}}\mathbf{V}. \tag{7}$$

A matrix containing the POD coefficients, $\mathbf{A}$, can then be formed as $\mathbf{A} = \mathbf{CV}$, where each column of this matrix contains the POD coefficients α_{ik}, where the subscript k denotes the k-th POD mode and subscript i denotes the i-th snapshot coefficient of POD mode k. Each snapshot i can then be reconstructed as,

$$\hat{\mathbf{p}}_i = \bar{\mathbf{p}} + \left(\sum_{k=1}^{R} \alpha_{ik}\phi_k \right). \tag{8}$$

The accuracy is dependent on the number R of POD modes retained in the expansion. An approximation on the accuracy of the reconstructed snapshots (in $E\%$) may be approximated by using the first R (with $R \leq N$) POD modes, such that,

$$\frac{\sum_{k=1}^{R} \lambda_k}{\sum_{k=1}^{N} \lambda_k} > \frac{E}{100}. \tag{9}$$

Higher Order Dynamic Mode Decomposition (HODMD)

Higher order Dynamic mode decomposition (HODMD) decomposes the spatio-temporal data, organised in snapshots ($\mathbf{p}_k$ is the data collected at time t_k), as a Fourier expansion of DMD modes:

$$\mathbf{p}_k \approx \mathbf{p}_k^{DMD} = \sum_{n=1}^{N} a_n \mathbf{u}_n e^{(\delta_n + i\omega_n)t_k}, \qquad k = 1, \ldots, K, \tag{10}$$

where $\mathbf{u}_n$ are the DMD modes. These modes are weighted by an amplitude, a_n, they grow or decay in time by a growth rate, δ_n, and oscillate with a frequency, ω_n. The number of DMD modes retained, N, can be referred to as the spectral complexity, while K is the temporal dimension, which generally represents the number of snapshots available for the decomposition. In HODMD, the data in eq.3 are equidistant in time, with time step Δt.

The algorithm of HODMD is described in detail in (Le Clainche and Vega 2017a), but it can be summarised in two main steps: (1) a spatial reduction and (2) the DMD-d algorithm. Initially, the spatio-temporal data are collected into a snapshot matrix as outlined in eq.3. For the first step, a singular value decomposition (SVD) is applied to reduce the spatial redundancies, i.e. to remove noise in experimental data or to retain the large scale structures in the case of complex or turbulent flows. The number of SVD modes retained in HODMD is defined automatically with a tunable tolerance ε_1 as in eq.9. Then, the DMD-d algorithm (the second step) is applied. This algorithm uses d time-delayed snapshots, resulting in a sliding window process, similar to the power spectral density (PSD) analysis. The parameter d is tunable, as well as a new tolerance ε_2, which defines the DMD modes retained in the expansion eq.10. HODMD will be applied to identify the main structures in the non-linear simulation of the turbulent flow. As presented in multiple examples in the literature (e.g. see (Vega and Le Clainche 2021)), HODMD is the appropriate tool, as the data analysed are turbulent and highly complex. With this algorithm, the main frequencies and modes driving the flow dynamics, which generally represent flow instabilities, will be identified (Le Clainche et al. 2020).

In what follows, the accuracy of the approximation of the original database ($\mathbf{p}_k^{DMD}$), using the DMD expansion eq. (10), will be measured in terms of the relative root mean square (RRMS) error as

$$\text{RRMS error} = \sqrt{\frac{\sum_{k=1}^{K} \|\mathbf{p}_k^{DMD} - \mathbf{p}_k\|_2^2}{\sum_{k=1}^{K} \|\mathbf{p}_k\|_2^2}}. \quad (11)$$

RESULTS AND DISCUSSION

CFD Simulation Results - Time-Dependent Flow Field

The unsteady aerodynamic flow field data was exported at 507 time instances, where each time-dependent three-dimensional flow field was written at every time step. Overall the total time of the exported unsteady data was over 3 times the largest vortex shedding period. The exported data were used to perform a detailed analysis on the evolution of unsteady vortical structures, around the main wing and the tailplane.

From these results, the computed flow was found to be highly unsteady and dominated by large-scale vortex shedding from the main wing. The unsteady features with significant vortical fluctuations can clearly be seen in Figure 4, which shows the time development of tubular vortical structures in terms of the iso-surfaces of the second invariant of the velocities (Q-criterion) (Jeong and Hussain 1995).

Two important unsteady features are evident from the figure: firstly, the vortices shed from the main wing are seen to completely cover the tailplane. This feature clearly suggests that the tailplane's effectiveness may be affected by the separated flow from the main wing. Although, the tailplane wake only indicates partial tailplane stall, thus retaining longitudinal stability, which is evidenced in flight by the pitching moment changes during the stall recovery. Secondly and more importantly, the shed vortices from the outboard of the main wing (region outside the mid-span) are seen to convect inward (negative z-direction) as they travel downstream before reaching the tailplane. This is thought to be related to the fuselage interaction on the pressure field, but also due to the wing spanwise loading profile. The Slingsby wing outer section has a shorter chord and a NACA 23013 profile when compared to a NACA 23015 at the root. The wing also has "washout" with 3° incidence at the root reducing to 0.33° at the tip. This may be a contributing factor driving the pressure gradient and observed inboard vortex convection. This spanwise convection has also been reported in flight by one of the authors on a similar aircraft when using smoke visualisation (Hoff and Gratton 2013).

The outboard vortical structure (marked by a black oval) is seen to meet the vortical structure shed from the wing root at the tailplane. This indicates the presence of a highly three-dimensional flow field characterised by rolling and twisting of vortical structures which impact the aircraft tailplane. A more quantitative study of these variations may be obtained by analysing the frequency content of the pressure time-history data. This has been done by outputting the power spectrum of the time signal. Subsequent POD and HODMD analyses have been carried out in the indicated sample in Figure 1. Figure 5 shows the computed power spectrum for the transient pressure signal in the form of a spectrogram, for the case when the angle of attack was $\alpha = 16°$. The data correspond to sampling points located at the final third of the main wing chord, and its spanwise location is inboard of the midspan. From the figure, the presence of two dominant frequencies, which are close together, is clearly evident. After performing the detailed analysis of the evolution of 3D unsteady structures, the results suggest that the two frequencies in this power spectrum correspond to the shed vortices from the root and tip regions of the main wing, which were observed to be arriving at the tailplane. It is worth mentioning here that the flow visualisation showed that the vortices take approximately the same time to reach the tailplane, although the outboard structure travels a longer distance, resulting in the closely-spaced frequencies. It must also be highlighted that further detailed monitoring is needed near the tailplane, to capture the interaction of the shedding from the inboard & outboard positions of the main wing, to assess whether there is any non-linear coupling between the modes. This non-linear analysis will be the subject of further research.

Finally, these two closely-spaced frequencies are close to the first tailplane structural natural frequency found in the experiments (Section **Flight Test Data**). The small difference found between the frequencies calculated numerically and experimentally is thought to be related to the noise generally found in experimental measurements, especially in flight tests, where the level of noise can reach values of up to 30% compared to the real signal (see (Mendez et al. 2021)). This error is quantified with the relative error,when comparing both frequencies: $f_{exp} = 9.4Hz$, $f_{num} = 11Hz$, relative error $= 17\%$. This error is assumed in the remaining of the article.

POD modes of the Transient Flow Field

POD analysis was performed on the transient flow field predicted by the time accurate DES simulation at an x-y plane, which extends from the wing trailing edge to the tailplane leading edge in x, over $y = +1.5$m to $y = -0.5$m, at z position corresponding to 10% of the wing span from the wing root (see Figure 1b, Plane 1). The cumulative sum of the normalized energy of the first 26 modes is plotted in Figure 6. Here, the sum of the energy in the first 9 modes accounts for 99.9% of the energy. This corresponds to $E = 99.9\%$ in eq.9. This analysis has therefore shown that most of the flow 'energy' was concentrated in the first few spatial modes, and that a modal approach to the prediction of the transient flow is capable of capturing the key features of the unsteadiness in the flow field.

A reconstruction of the pressure snapshots was also performed to test how well the POD modal description of the flow represented the actual flow physics. The transient pressure snapshot was reconstructed using the expansion given by eq.8, and in this particular case only the first 9 modes were used (i.e. $R = 9$ in eq.8). The result is plotted in Figure 7 along with the original snapshot from the CFD. It was found that the accuracy of the reconstructed snapshots improved with increasing the number of POD modes retained, as expected. Although there were also regions of discrepancies in the reconstruction (e.g. high-pressure area in the right)in Figure 7 and this may be due to the truncation of higher wavenumber modes in the reconstruction. However, this does not alter the essential characteristics of the flow features, which are preserved well in the POD results. Finally, the temporal coefficients of the three first POD modes have been analysed with a Fast Fourier Transform (FFT). Figure 8 shows that the main frequency of the modes analysed is $11.7Hz$. This frequency is closely related to one of the two frequencies found in the spectrogram of the CFD simulation.

Higher-Order Dynamic Mode Decomposition Results

In addition to the POD analysis performed in the previous section, further analysis of the unsteady CFD simulation, as outlined in the first section of the results, was performed using

HODMD. Specifically, HODMD has been applied to analyse two sets of databases, one set corresponding to three different $x-y$ (streamwise – normal component) planes, situated at (spanwise component) $z = 0.89$m, 1.66m and 5.32m, corresponding to 10% (Plane 1), 25% (Plane 2) and 98.5% (Plane 3) of the wing span from the wing root (see Figure 1b), with plane 3 extending in x to the tailplane leading edge tip. ; and another set related to three $y-z$ planes, situated at $x = 1.52$m, 2.21m and 3.41m. The three planes are placed such that the first plane is immediately behind the wing trailing edge, the third plane is immediately in front of tail plane and the second plane is at a distance $\approx 40\%$ of the distance between the first and third plane. As in the previous case, each database is also composed of 507 snapshots equidistant in time with $\Delta t = 6.7 \times 10^{-4} s$.

In the following results, HODMD has been specifically calibrated to maximise the accuracy of the reconstruction of the snapshot matrix following the DMD expansion presented in eq.10. To achieve this, the algorithm has been solved by tuning the value of the parameter $d \in [50, 250]$ and the parameters $\varepsilon_1 = \varepsilon_2$ to 10^{-3} and 10^{-4} providing both, coarse and fine results, respectively, which are robust (the method retains similar DMD modes using these calibrations, to represent the flow physics). Figure 9 shows the frequencies as a function of the amplitudes for the two analysed databases, $x-y$ planes on top, and $y-z$ planes on the bottom part of the figure, using several calibration parameters. The analysis of the first case identifies the main frequency f' with $11.78Hz$, its sub-harmonic $f'/2$ with $5.89Hz$, the interaction between the first two modes, defined with frequency $f' + f'/2$, at $17.67Hz$, and the first harmonic mode of the main frequency $2f'$ with $23.55Hz$. As well as in the analysis of the temporal coefficients of the POD modes, a careful examination of this main frequency revealed that it is related to one of the two frequencies shown on the spectrogram of Figure 5 (this frequency is near $12Hz$ on the spectrogram and $f' = 11.77Hz$ calculated with HODMD).

The analysis of the second case shows the presence of a new frequency, $f^* = 13.37Hz$. This new frequency is in line with the results from the spectrogram in Figure 5 and with the experiments, where it showed the presence of two leading closely-spaced frequencies at $f \approx 12Hz$ (mentioned before) and $f \approx 13Hz$. Both the spectrogram analysis above (Figure 5) and the HODMD analysis have shown the presence of this new frequency, suggesting that the presence of this frequency could be connected to the non-linear coupling of the modes in the flow field. Further research is necessary to confirm this complex unsteady phenomenon.

In Figure 10, the main DMD modes extracted from the analysis of the $x - y$ planes are shown. Here it is evident that the y and z velocity components clearly show the downstream movement (along $x-$axis) of the dominant vortex structures and the streamwise velocity component map also highlights this feature, with a positive velocity along the vortex sheet. It is possible to follow the position of the highest intensity area from the y and z velocity components along the three different planes studied, showing the convenction characteristics of the wake flow. Finally, the leading mode also shows a decrease in the pressure with increasing streamwise position (on the wake behind the wing). Similarly, the results on the first two $x - y$ planes also show similar flow features, as they represent different parts of the wake behind the wing. On the other hand, the last plane shows the movement of the main vortex near the tip of the wing, which is a feature that also appears in the results of the shed vortices (Figure 4).

Figure 11 compares the streamwise velocity in the leading modes identified by the method (f', $f'/2$, $f' + f'/2$ and $2f'$). As expected, the sub-harmonic mode shows similar structures as the main mode, but with a larger size. This is a common feature, generally identified in periodic dynamics (Vega and Le Clainche 2021). The same explanation can be extended to the structures of the first harmonic with frequency $2f'$. In this case, the harmonic is similar to the main mode, but the size of the structures is smaller. Finally, the shape of the mode with frequency $f' + f'/2$, which represents the modal interaction between the leading frequency mode and its sub-harmonic, is a combination of the aforementioned two modes.

Comparable to the analysis presented above on the $x - y$ planes, HODMD analysis was also performed on the $y - z$ planes as shown in Figures 12 and 13. The new frequency mode

f^* is compared with the leading frequency mode f', also identified in the previous analysis. The highest intensity of the DMD mode related to this new frequency f^* (Figure 12) is mainly centred around the wingtip vortex, characterising its movement. This vortex rotates on the $y-z$ plane, so the velocity components corresponding to these axes show the rotation in all the planes. The streamwise velocity component mainly shows the movement of the wake behind the wing. Moreover, the pressure field shows two pressure drops, one due to the fuselage interaction (low $z-$coordinate) and one on the wingtip vortex.

Finally, the shape of the leading frequency mode, f', calculated in this plane (Figure 13), highlights its connection to the main wing vortex shedding frequency. It is important to mention that, in all the analysed results, thus far, it is clear that the unsteady flow field is highly three-dimensional, as the structures appearing on this mode are characterised by the presence of the three components of the velocity. The pressure field only shows the fuselage interaction on this mode. These analyses thus have indicated the presence of a complex non-linear coupling of the multiple modes.

Figure 14 shows the reconstruction of the original databases of the streamwise velocity component and pressure field. It can be seen that when using the modes obtained, the algorithm can reconstruct the data. The error obtained in the process has been calculated with eq. 11, obtaining an RRMS error of 2% for the $x-y$ planes and 2.17% for the $y-z$ planes.

It should be noted that, although the complexity of the flow analysed is very high, the number of patterns describing the flow dynamics is small. The general flow dynamics is represented by a leading frequency mode f' and its non-linear interactions, representing the vortex shedding, modelling the wake behind the wing, and a new mode f^*, which is connected to the wingtip vortex. This information offers the potential to develop reduced-order models describing the flow physics in this complex problem. This will be the topic for future research.

CONCLUSIONS

This paper has presented a detailed analysis of DES CFD results from the transient flow field of a Slingsby light aircraft in stall conditions. A study of the unsteady flow structures showed the presence of a highly three-dimensional complex flow structure, where the vortices shed from the root and tip regions of the main wing were observed to converge downstream at the fore of the tailplane, and then convect towards the tailplane. Since the vortices travelling from the wing tip cover comparatively longer distances, they were found to travel faster than the root vortices. This characteristic manifested itself as two closely separated shedding frequencies in the unsteady power spectrum. The flow visualisation also showed 3D rolling and twisting of the vortical structures as they travelled downstream.

Dynamic modelling of the unsteady flow has also been investigated by using POD and HODMD. The POD analysis was applied specifically to the unsteady pressure field as this exerts higher aerodynamic loads on the wing surfaces and is, therefore, of the most relevance for the flow around wings, in stall conditions. The method was used to reconstruct the unsteady pressure snapshot from a weighted addition of POD bases, and the results showed that the reconstruction was capable of retaining all the salient features of the unsteady flow.

Additionally, HODMD method was applied to both the velocity and the pressure fields. The method was shown to identify the main flow structures driving the flow dynamics. More specifically, the oscillating frequencies leading the motion of the three-dimensional rolling and twisting of the vortical structures have been successfully identified, highlighting the flow instabilities present in the flow.

POD also allows the reconstruction of an unsteady snapshot of the 3D unsteady flow field, which would be important for reconstructing the flow field at any arbitrary time instance. The temporal coefficients of POD also shows the main frequency leading the motion of the flow.

Further, the unsteady analysis fidelity offered by HODMD was able to capture the all the important unsteady modes in the flow field. The main dynamics modelling the flow are represented by a mode modelling the vortex shedding in the wake behind the wing and its harmonics and another mode modelling the wingtip vortex shedding. This result could be combined in future research with flow control strategies. Moreover, the flow physics of the highly complex flow studied here can be represented by a reduced number of DMD modes, thus offering the potential to develop a reduced-order model. This will be the topic of future research by the authors.

DATA AVAILABILITY

Codes are available on-line in `https://data.mendeley.com/datasets/z8ks4f5vy5/1`. The data will be shared upon request.

ACKNOWLEDGEMENTS

A.C. and S.L.C. acknowledge the grant PID2020-114173RB-I00 funded by MCIN/AEI/ 10.13039/501100011033. A.C. acknowledges the support of Universidad Politécnica de Madrid, under the programme 'Programa Propio'.

NOTATION

$x - y - z$	=	aircraft axes;
α	=	angle of attack;
ρ	=	air density;
ν	=	efficiency;
ω	=	engine rotational speed;
γ	=	flight path descent angle;
AR	=	wing aspect ratio;
ADC	=	air data computer;
CFD	=	computational fluid dynamics;
DES	=	detached eddy simulation;
EAS	=	equivalent airspeed;
HODMD	=	higher-order dynamic mode decomposition;
POD	=	proper orthogonal decomposition.

REFERENCES

Alexander, M. G., Harris, F. K., Spoor, M. A., Boyland, S. R., Farrell, T. E., and Raines, D. M. (2016). "Active flow control (afc) and insect accretion and mitigation (iam) system design and integration on the boeing 757 ecodemonstrator." *16th AIAA Aviation Technology, Integration, and Operations Conference*.

Bennett, C. J. and Lawson, N. J. (2018). "On the development of flight-test equipment in relation to the aircraft spin." *Progress in Aerospace Sciences*, 102, 47–59.

Berkooz, G., Holmes, P., and Lumley, J. L. (1993). "The proper orthogonal decomposition in the analysis of turbulent flows." *Annual Review of Fluid Mechanics*, 25, 539–575.

Casadei, L., Könözsy, L., and Lawson, N. J. (2019). "Unsteady detached-eddy simulation (des) of the jetstream 31 aircraft in one engine inoperative (oei) condition with propeller modelling." *Aerospace Science and Technology*, 91, 287–300.

Chatterjee, A. (2000). "An introduction to the proper orthogonal decomposition." *Current Science*, 78, 808–817.

Chen, H., Reuss, D. L., Hung, D. L., and Sick, V. (2012). "A practical guide for using proper orthogonal decomposition in engine research." *International Journal of Engine Research*, 14, 307–319.

Ciliberti, D., Vecchia, P. D., Nicolosi, F., and Marco, A. D. (2017). "Aircraft directional stability and vertical tail design: A review of semi-empirical methods." *Progress in Aerospace Sciences*, 95, 140–172.

Cordier, L. and Bergmann, M. (2008). "Proper orthogonal decomposition: an overview." *Lecture series 2002-04, 2003-03 and 2008-01 on post-processing of experimental and numerical data, Von Karman Institute for Fluid Dynamics*.

Frankhouser, M., Hird, K., Naigle, S., Gregory, J. W., and Bons, J. P. (2015). "Nanosecond dielectric barrier discharge plasma actuator flow control of compressible dynamic stall." *46th AIAA Plasmadynamics and Lasers Conference*.

Gardner, A. D., Wolf, C. C., and Raffel, M. (2019). "Review of measurement techniques for unsteady helicopter rotor flows." *Progress in Aerospace Sciences*, 111.

Grote, A. and Radespiel, R. (2006). "Studies on tailplane stall for a generic transport aircraft configuration." *44th AIAA Aerospace Sciences Meeting and Exhibit*.

Hall, R. M., Woodson, S. H., and Chambers, J. R. (2004). "Overview of the abrupt wing stall program." *Progress in Aerospace Sciences*, 40, 417–452.

Heinz, S. (2020). "A review of hybrid rans-les methods for turbulent flows: Concepts and applications." *Progress in Aerospace Sciences*, 114.

Higham, J. E., Brevis, W., and Keylock, C. J. (2016). "A rapid non-iterative proper orthogonal decomposition based outlier detection and correction for piv data." *Measurement Science and Technology*, 27.

Hoff, R. I. and Gratton, G. B. (2013). "Spin induced aerodynamic flow conditions on full-scale aeroplane wing and horizontal tail surfaces." *Aeronautical Journal*, 117, 1198.

Howard, C., Gupta, S., A., A., T.A.G., L., and D.F., F. (2017). "Proper orthogonal decomposition (pod) analysis of cfd data for flow in an axisymmetric sudden expansion." *Chemical Engineering Research and Design*, 123, 333–346.

Hu, C., Yang, C., Yi, W., Hadzic, K., Xie, L., Zou, R., and Zhou, M. (2020). "Numerical investigation of centrifugal compressor stall with compressed dynamic mode decomposition." *Aerospace Science and Technology*, 106.

Jeong, J. and Hussain, F. (1995). "On the identification of a vortex." *Journal of Fluid Mechanics*, 3, 69–94.

Lawson, N., Jacques, H., Gautrey, J., Cooke, A., Holt, J., and Garry, K. (2017). "Jetstream 31 national flying laboratory: Lift and drag measurement and modelling." *Aerospace Science and Technology*, 60, 84–95.

Le Clainche, S., Han, Z. H., and Ferrer, E. (2019). "An alternative method to study crossflow instabilities based on high order dynamic mode decomposition." *Physics of Fluids*, 31.

Le Clainche, S., Izbassarov, D., Rosti, M., Brandt, L., and Tammisola, O. (2020). "Coherent structures in the turbulent channel flow of an elastoviscoplastic fluid." *Journal of Fluid Mechanics*, 888.

Le Clainche, S., Sastre, F., Vega, J. M., and Velazquez, A. (2017a). "Higher order dynamic mode decomposition applied to post-process a limited amount of noisy piv data." *47th AIAA Fluid Dynamics Conference*.

Le Clainche, S. and Vega, J. M. (2017a). "Higher order dynamic mode decomposition." *SIAM Journal on Applied Dynamical Systems*, 16, 882–925.

Le Clainche, S. and Vega, J. M. (2017b). "Higher order dynamic mode decomposition to identify and extrapolate flow patterns." *Physics of Fluids*, 29.

Le Clainche, S., Vega, J. M., and Soria, J. (2017b). "Higher order dynamic mode decomposition of noisy experimental data: The flow structure of a zero-net-mass-flux jet." *Experimental Thermal and Fluid Science*, 88, 336–353.

Lumley, J. L. (1967). "The structure of inhomogeneus turbulent flows." *Atmospheric Turbulence and Radio Wave Propagation*, 166–177.

Lutz, T., Gansel, P. P., Waldmann, A., Zimmermann, D. M., and Hülse, S. S. A. (2015). "Time-resolved prediction and measurement of the wake past the crm at high reynolds number stall conditions." *53rd AIAA Aerospace Sciences Meeting*.

Lutz, T., Gansel, P. P., Waldmann, A., Zimmermann, D. M., and Hülse, S. S. A. (2016). "Prediction and measurement of the common research model wake at stall conditions." *Journal of Aircraft*, 53, 501–514.

Mallik, W. and Raveh, D. E. (2020). "Aerodynamic damping investigations of light dynamic stall on a pitching airfoil via modal analysis." *Journal of Fluids and Structures*, 98, 103111.

Mendez, C., Le Clainche, S., Moreno-Ramos, R., and Vega, J. M. (2021). "A new automatic, very efficient method for the analysis of flight flutter testing data." *Aerospace Science and Technology*, 114.

Menter, F. and Kuntz, M. (2003). "A zonal sst-des formulation." *DES Workshop*.

Menter, F. R. (1994). "Two-equation eddy-viscosity turbulence models for engineering applications." *AIAA Journal*, 32, 1598–1605.

Mohan, A. T., Visbal, M. R., and Gaitonde, D. V. (2015). "Model reduction and analysis of deep dynamic stall on a plunging airfoil using dynamic mode decomposition.

Neves, A. F., Lawson, N. J., Bennett, C. J., Khanal, B., and Hoff, R. I. (2020). "Unsteady aerodynamics analysis and modelling of a slingsby firefly aircraft: Detached-eddy simulation model and flight test validation." *Aerospace Science and Technology*, 106.

Nichols, R. H. (2006). "Comparison of hybrid turbulence models for a circular cylinder and a cavity." *AIAA Journal*, 44, 1207–1219.

Okonkwo, P. and Smith, H. (2016). "Review of evolving trends in blended wing body aircraft design." *Progress in Aerospace Sciences*, 82, 1–23.

Phillips, W. F. (2010). *Mechanics of flight*. Wiley, second edition.

Rao, D. V. and Go, T. H. (2019). "Optimization of aircraft spin recovery maneuvers." *Aerospace Science and Technology*, 90, 222–232.

Raymer, D. P. (1999). *Aircraft design : a conceptual approach*. American Institute of Aeronautics and Astronautics, third edition.

Rizzi, A., Eliasson, P., McFarlane, C., Goetzendorf-Grabowski, T., and Vos, J. (2010). "Virtual-aircraft design & control of transcruiser - a canard configuration." *AIAA Atmospheric Flight Mechanics Conference 2010*.

Rona, A. and Brooksbank, E. J. (2003). "Pod analysis of cavity flow instability." *Proceedings of the 41st Aerospace Sciences Meetings and Exhibit*.

Sinha, N., Dash, S. M., Chidambaram, N., and Findlay, D. (1998). "A perspective on the simulation of cavity aeroacoustics." *36th AIAA Aerospace Sciences Meeting and Exhibit*.

Sirovich, L. (1987). "Turbulence and the dynamics of coherent structures. ii. symmetries and transformations." *Quarterly of Applied Mathematics*, 45, 573–582.

Spalart, P. (2001). "Young-person's guide to dettached-eddy simulation grids.

Spalart, P. and Allmaras, S. (1997). "Comments on the feasibility of les for wings, and on a hybrid rans/les approach." Proceedings of first AFOSR international conference on

DNS/LES, Ruston, Louisiana, USA.

Spalart, P. R., Deck, S., Shur, M. L., Squires, K. D., Strelets, M. K., and Travin, A. (2006). "A new version of detached-eddy simulation, resistant to ambiguous grid densities." *Theoretical and Computational Fluid Dynamics*, 20, 181–195.

Teng, T., Zhang, T. S., Liu, S. F., and Grant, P. R. (2015). "Representative post-stall modeling of t-tail regional jet and turboprop aircraft for flight training simulator." *AIAA Modelling and Simulation Technologies Conference*.

Teng, T. T., Zhang, T. S., and Grant, P. R. (2016). "Semi-analytical and empirical approaches to aircraft configuration effects on post-stall aerodynamics." *AIAA Atmospheric Flight Mechanics Conference*.

Vega, J. M. and Le Clainche, S. (2021). *Higher order dynamic mode decomposition and its applications*. Academic Press, an imprint of Elsevier.

Wang, L. and Fu, S. (2017). "Detached-eddy simulation of flow past a pitching naca 0015 airfoil with pulsed actuation." *Aerospace Science and Technology*, 69, 123–135.

Zhou, L., Gao, Z., and Du, Y. (2019a). "Flow-dependent ddes/$\gamma - re_{\theta t}$ coupling model for the simulation of separated transitional flow." *Aerospace Science and Technology*, 87, 389–403.

Zhou, T., Dowell, E., and shan Feng, S. (2019b). "Computational investigation of wind tunnel wall effects on buffeting flow and lock-in for an airfoil at high angle of attack." *Aerospace Science and Technology*, 95.

List of Figures

a)

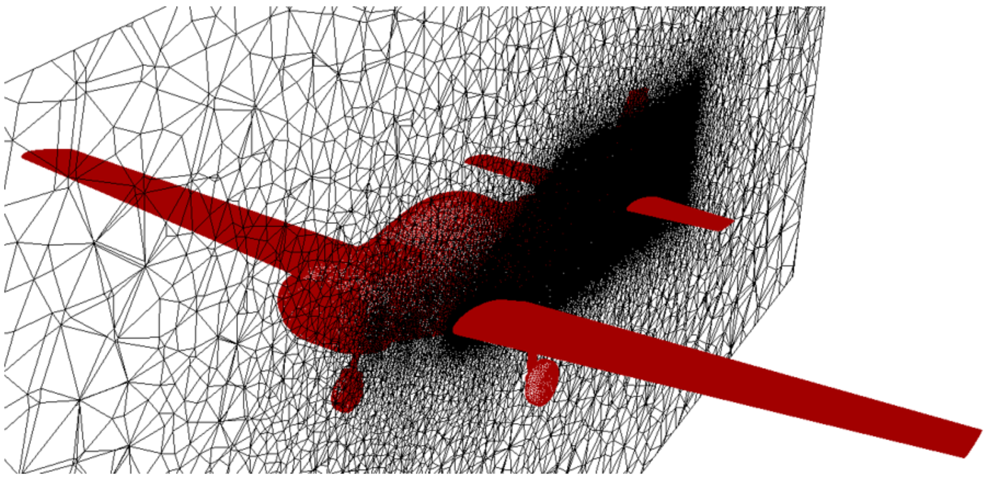

b)

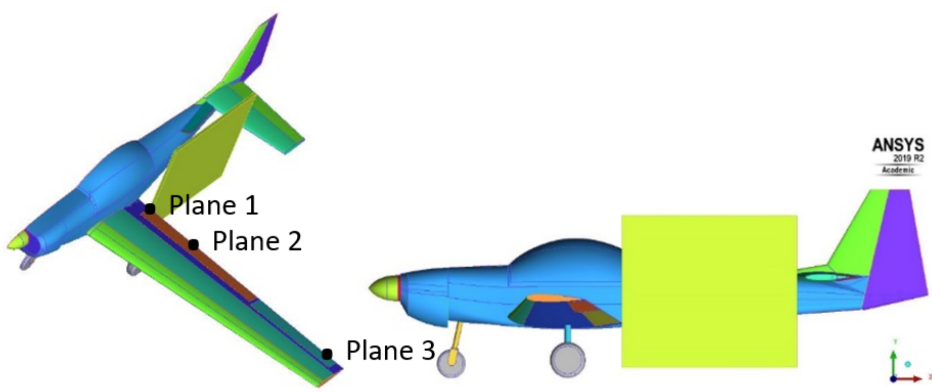

Fig. 1. CFD wake mesh and analysis planes. (a) Isotropic cells behind wing wake to facilitate DES solution (body mirrored for clarity). (b) POD analysis plane – Plane 1 (isometric and view side). The position of planes 2 and 3 is indicated for the sake of clarity.

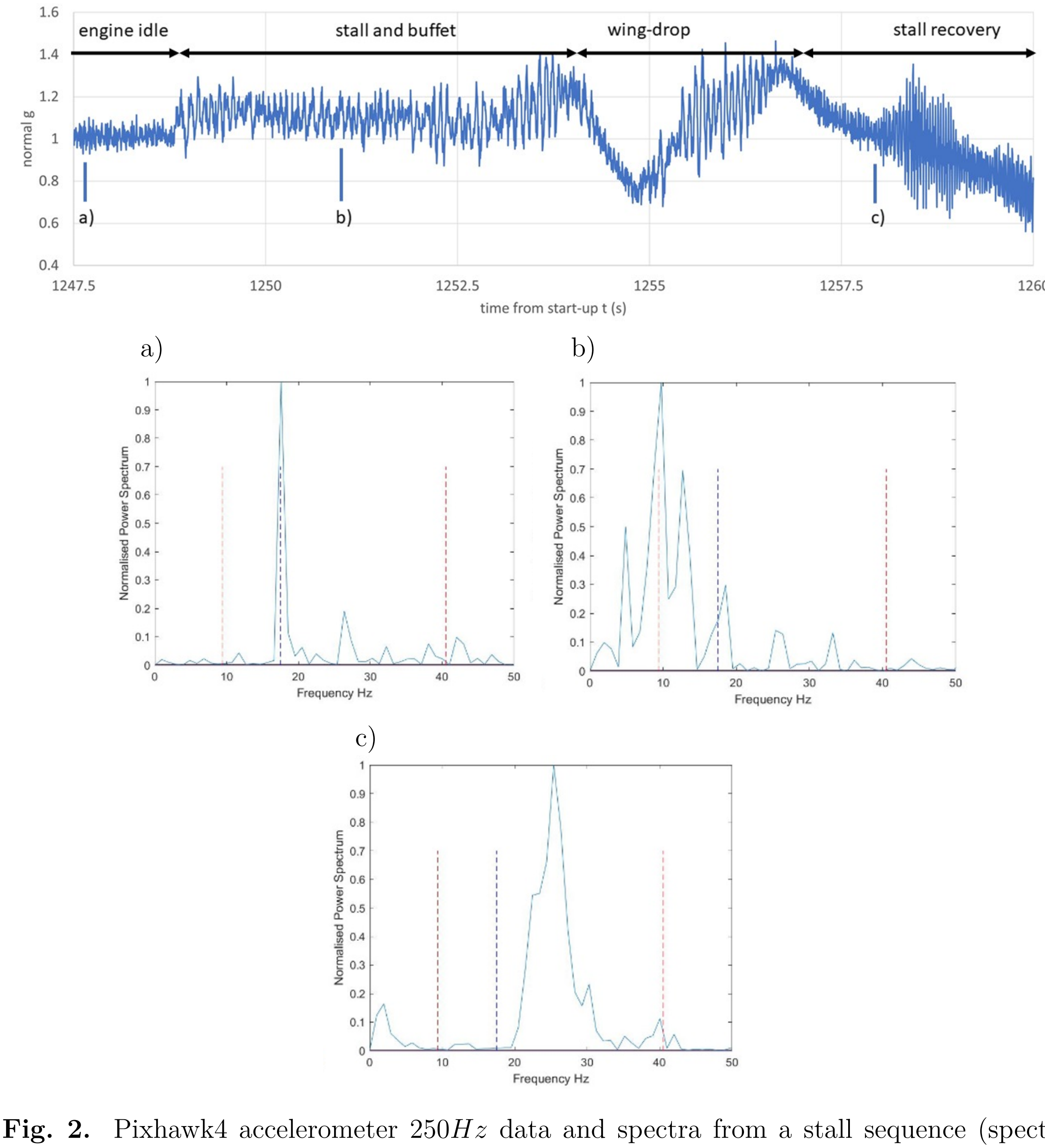

Fig. 2. Pixhawk4 accelerometer $250Hz$ data and spectra from a stall sequence (spectra red dashed lines indicate tailplane natural frequencies, blue dashed line indicates engine idle frequency a) engine idle spectra b) stall spectra c) spectra during aircraft stall recovery.

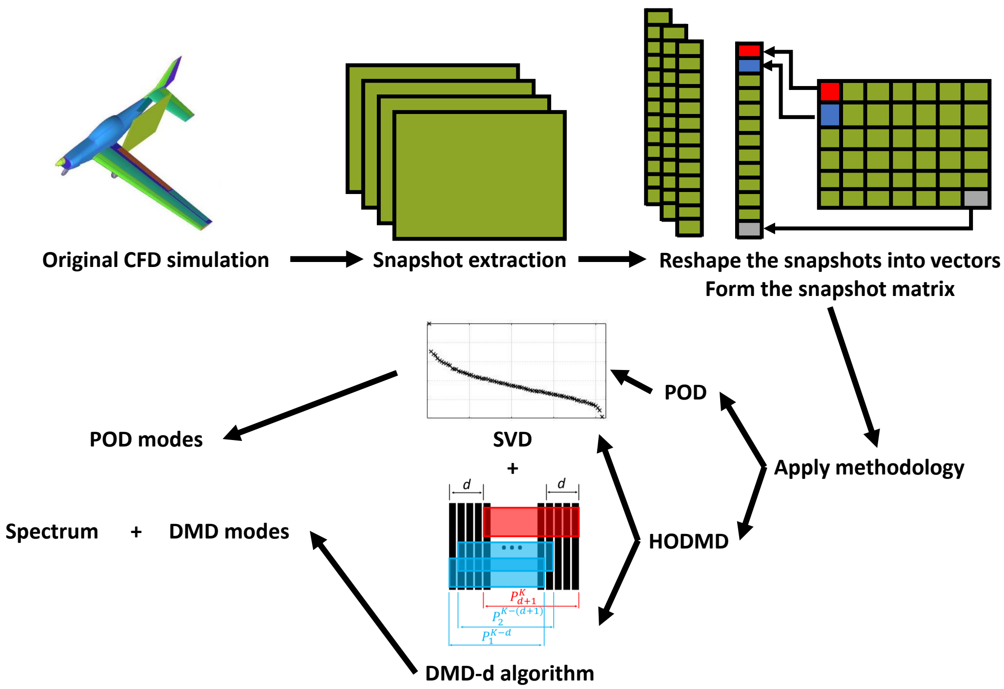

Fig. 3. Flowchart containing the process of the implemented steps in the methodology (POD and HODMD).

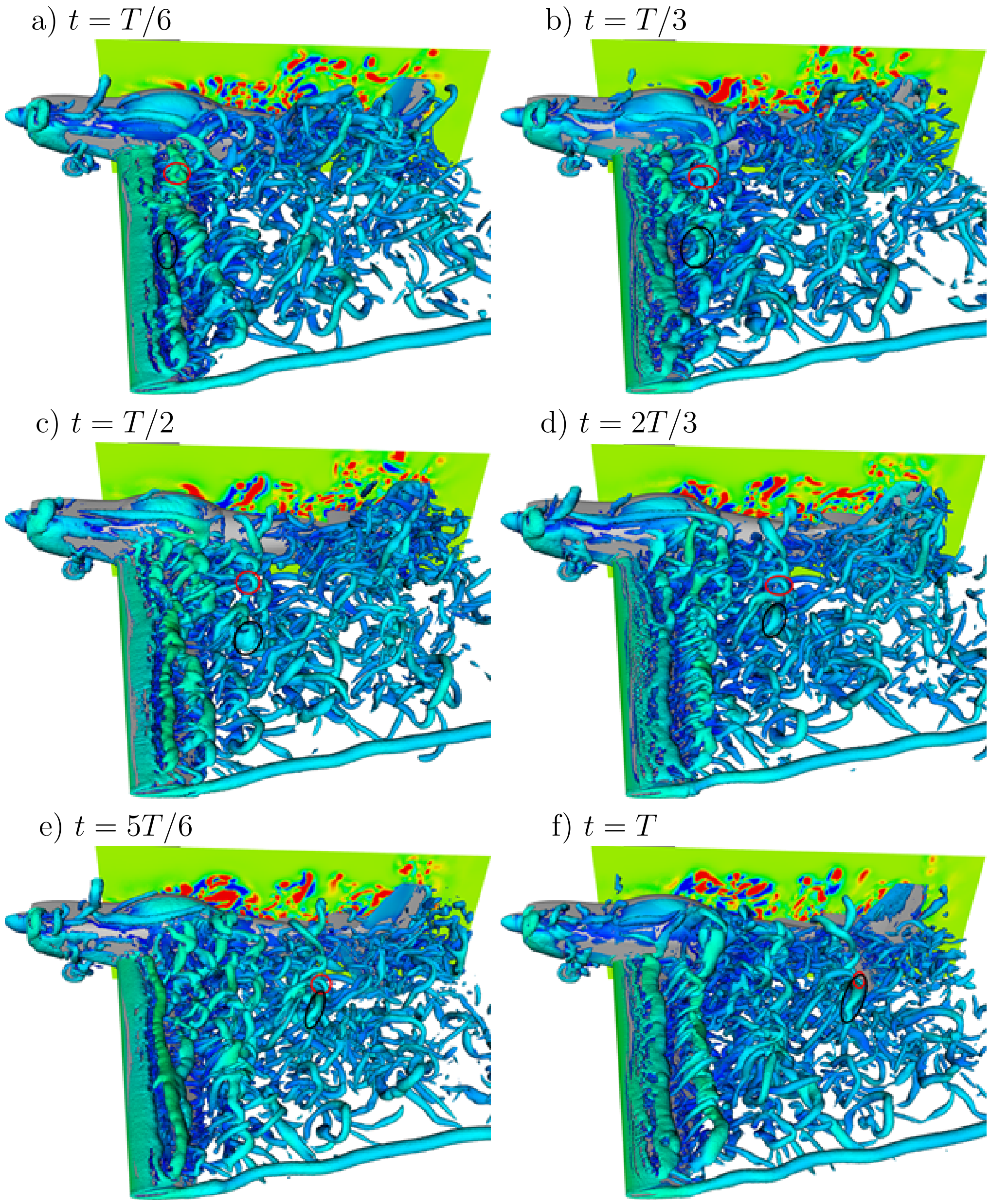

Fig. 4. Spectra Evolution of vertical structures over one cycle of oscillation: iso-contours of the Q-criterion (Here T is the time for shed vortices from main wing to reach the tailplane).

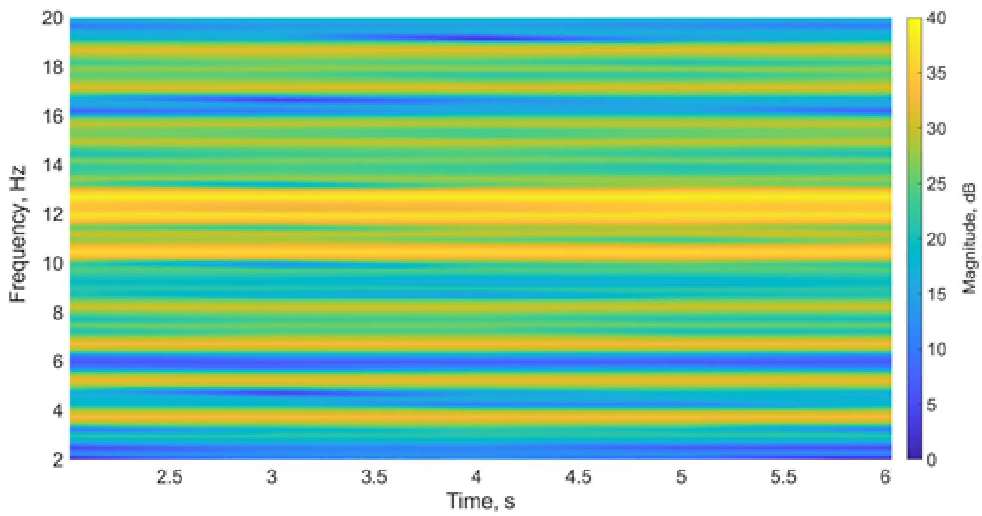

Fig. 5. Spectragram of the DES time signal from a representative point in the wake of the plane in the case with AoA of 16°, see details in (Spalart and Allmaras).

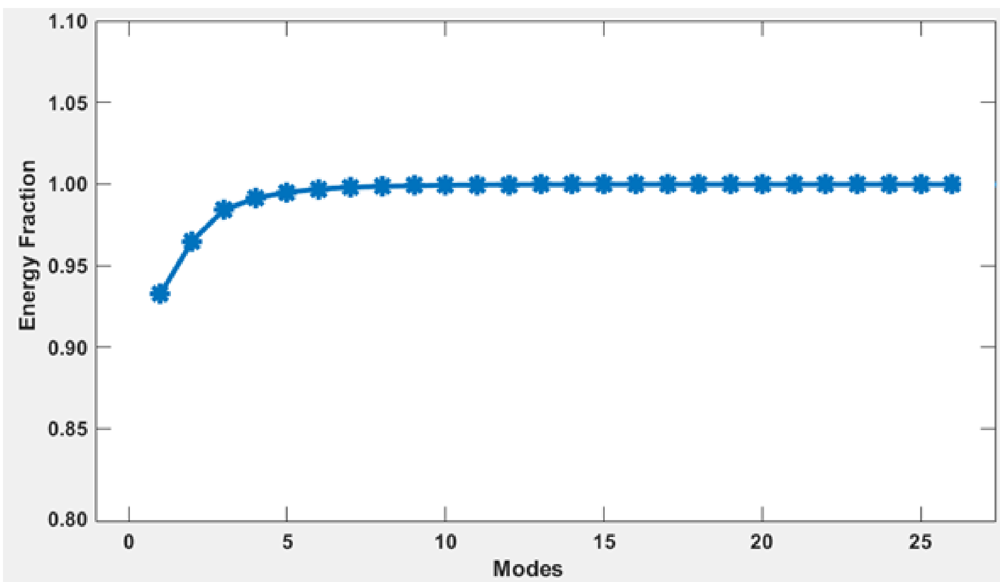

Fig. 6. Cumulative energy distribution of the first 26 most energetic modes.

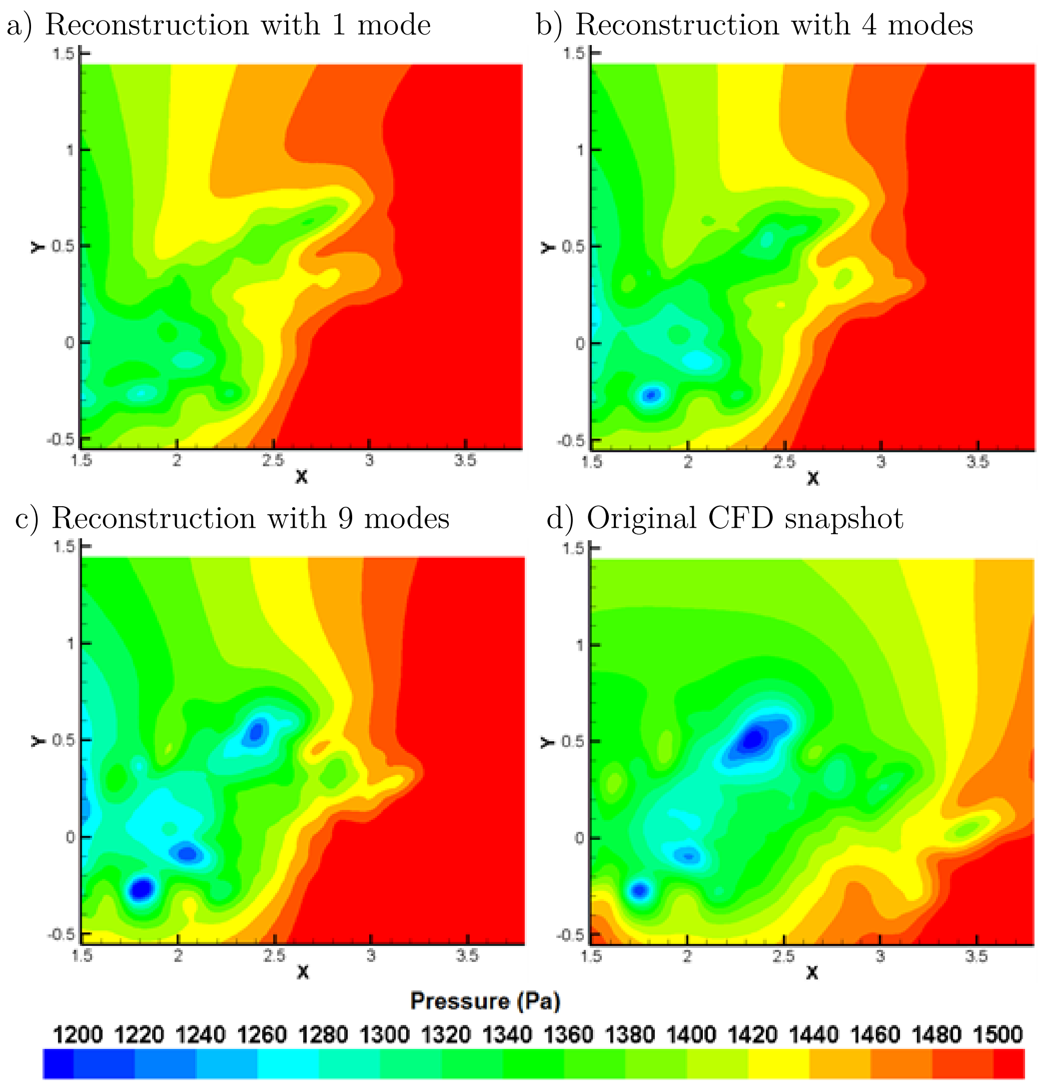

Fig. 7. Reconstructed snapshot of the unsteady pressure field at a representative time instant modelling the plane described in Figure 1b (Plane 1).

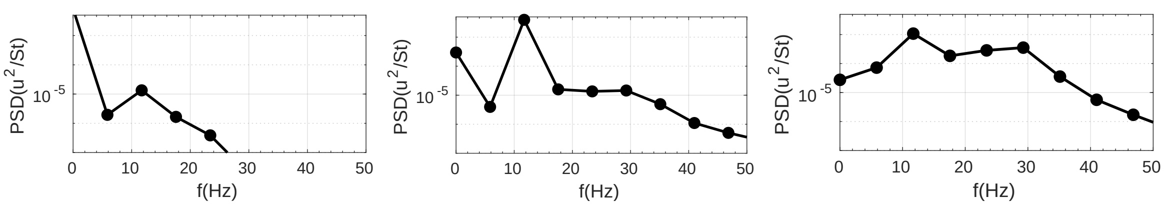

Fig. 8. Power spectrum of FFT scaled with the Strouhal number, applied to the temporal coefficients of the three first POD modes.

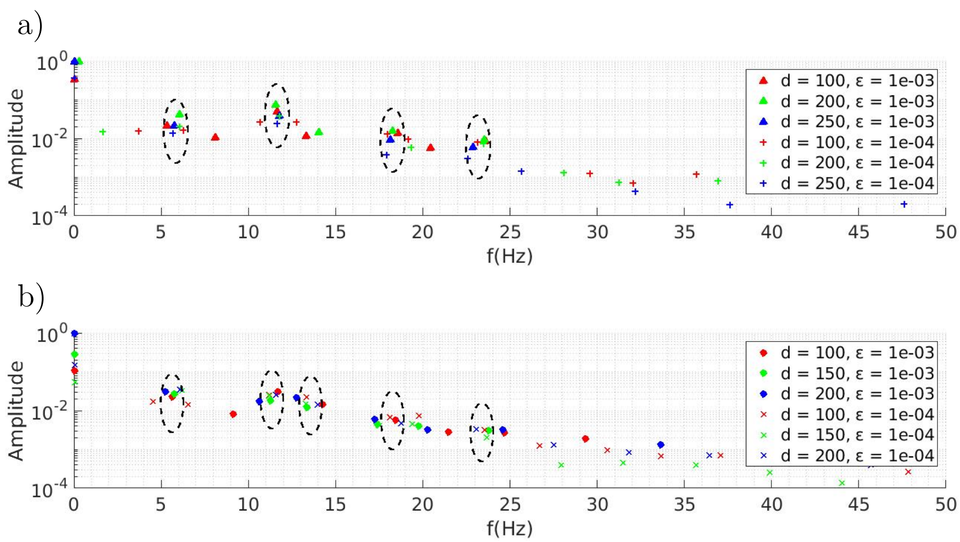

Fig. 9. Frequency vs. amplitudes representing the HODMD modes in the $x-y$ planes (a) and the $y-z$ planes (b) extracted in the wake of the airplane at $z = 0.89$, 1.66, 5.32 for (a) and $x = 1.52$, 2.21 and 3.41 for (b)

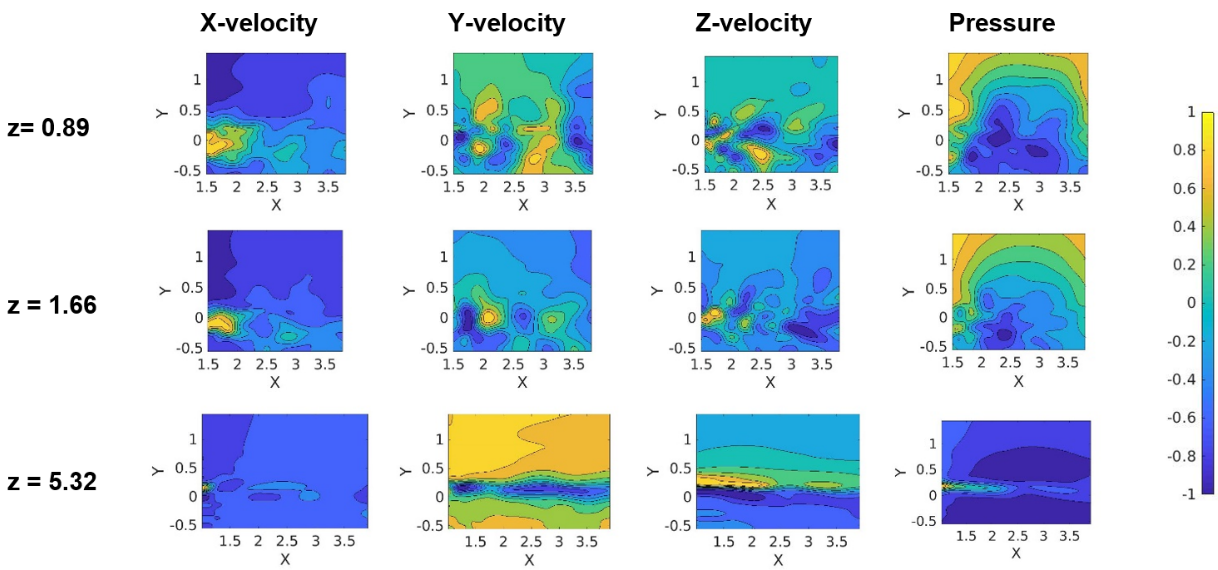

Fig. 10. Real part of the three velocity components and the pressure field of the main DMD mode ($f' = 11.78Hz$) calculated in three $x - y$ planes (for several values of z).

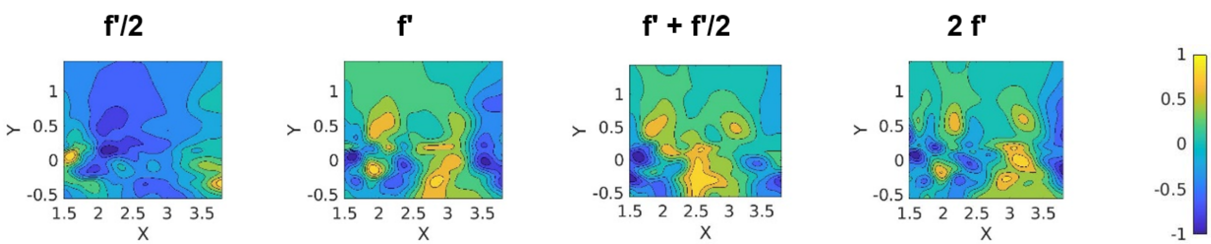

Fig. 11. Real part of the normal (y) velocity component of the most relevant DMD modes. The leading frequency is $f' = 11.78Hz$.

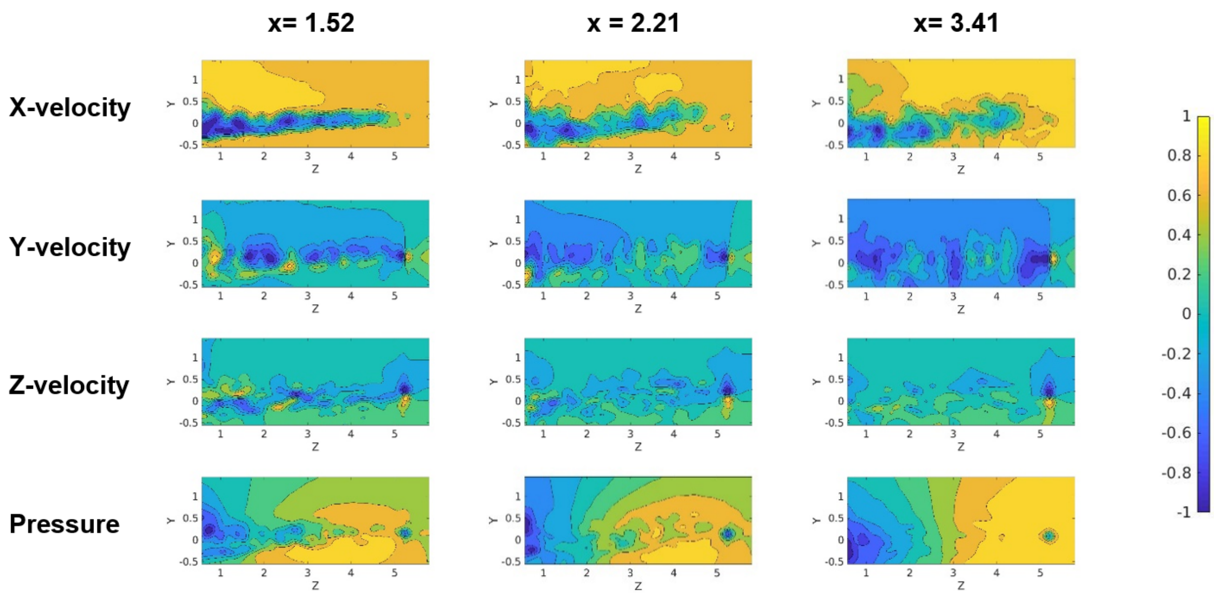

Fig. 12. Real part of the three velocity components and the pressure field of the new-frequency DMD mode ($f^* = 13.37Hz$) calulated in three $y - z$ planes.

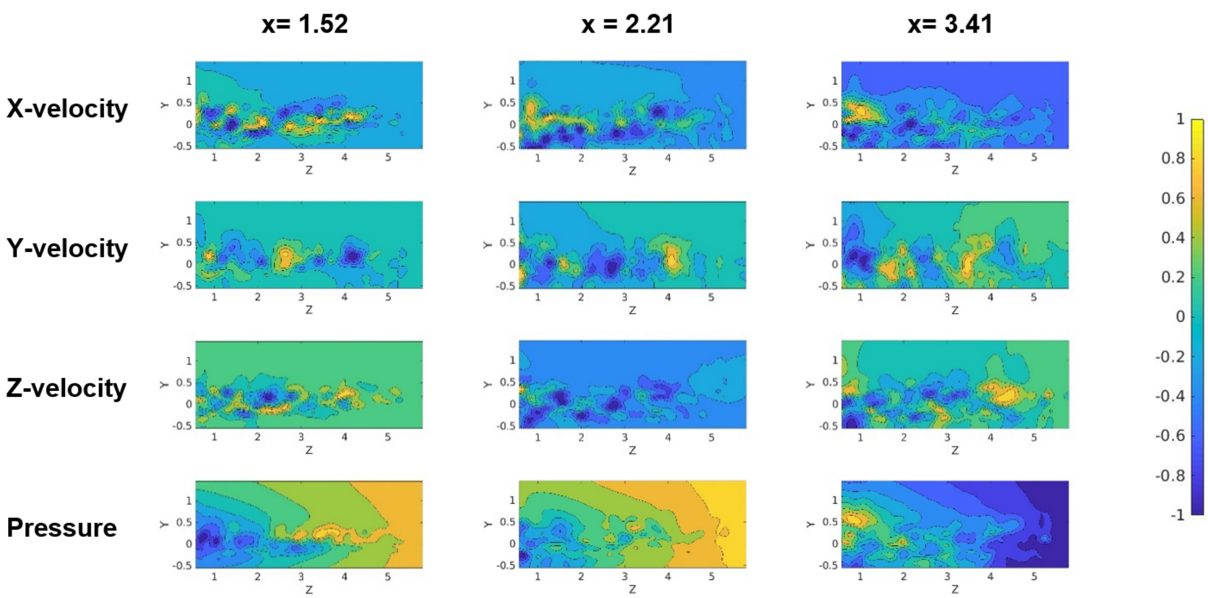

Fig. 13. Same as Figure 12 for the leading frequency mode, $f' = 11.78Hz$.

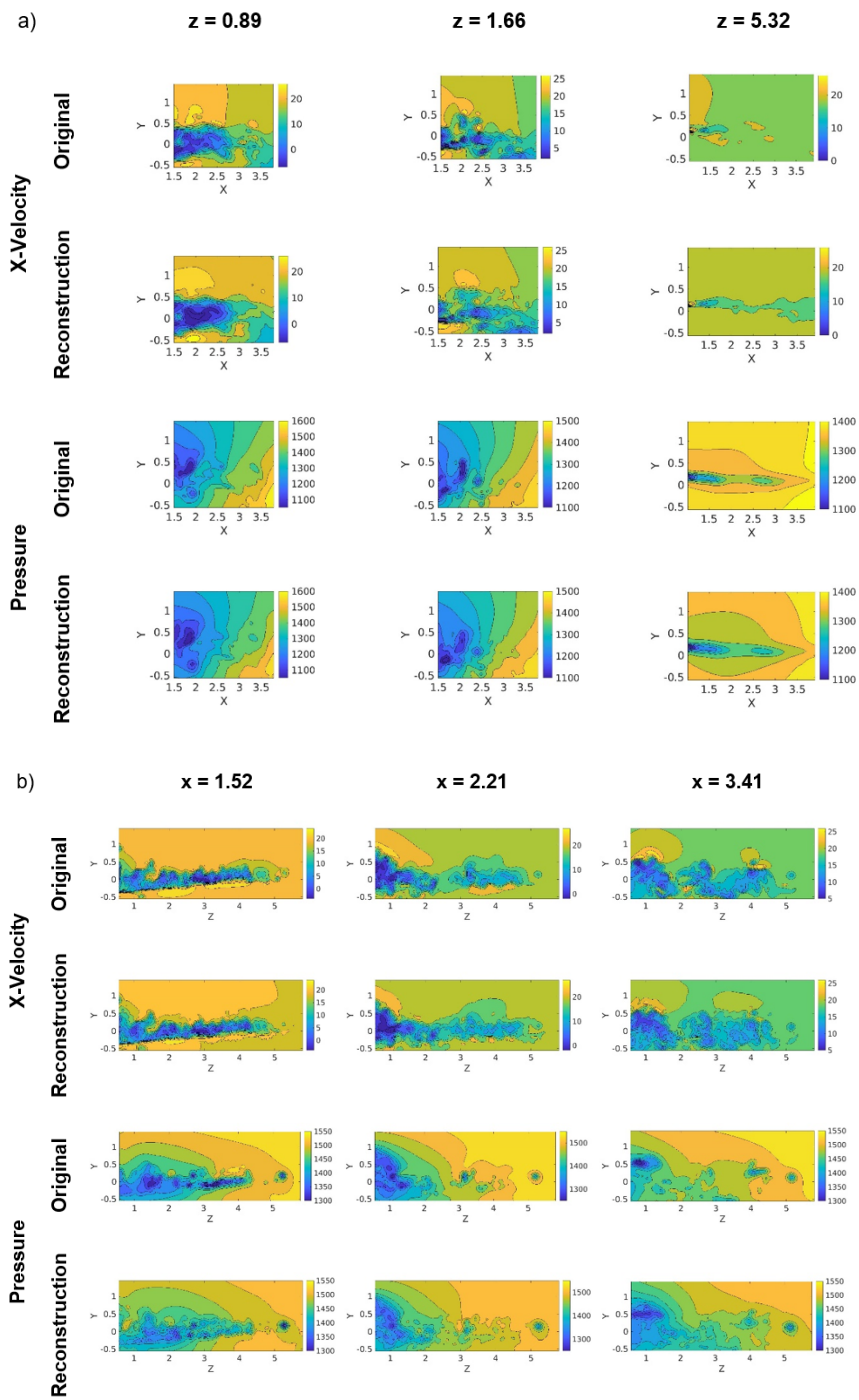

Fig. 14. Representative snapshot of the reconstructed planes after using HODMD for the streamwise velocity component and the pressure field. (a) $x - y$ planes. (b) $y - z$ planes.